

Simulating MCP secondary electron avalanche process by Geant4

Huaxing Peng^{a,b}, Baojun Yan^{1a,b}, Han Miao^{2a,c}, Shulin Liu^{a,b,c}, Binting Zhang^{a,b}

^a*Institute of High Energy Physics, Beijing 100049, People's Republic of China*

^b*State Key Laboratory of Particle Detection and Electronics, Beijing, 100049, People's Republic of China*

^c*University of Chinese Academy of Sciences, Beijing 100049, People's Republic of China*

Abstract

The curved channel Microchannel Plates(MCP) represent a significant advancement in inhibiting ion-feedback, which is the major cause of after-pulse in output signal of MCPs. Many high sensitive experiments, such as neutrino detection, require as low noise as possible. The conventional straight channel MCP is inevitable to introduce the after-pulses, which are the major source of noise. Normally, couple two straight MCPs in cascade and combine the channels into a "V" shape can effectively suppress ion-feedback, known as chevron MCPs. However, due to the limitation manufacture technology, the gap always exist. It will worsen the resolution and peak-to-valley ratio. Different with the joint MCPs that is mentioned above, the curved MCPs exhibit superior characteristics. Based on the Geant4 Monte Carlo simulation framework, we investigate how the geometrical parameter of curved channel MCP influence the gain. Consequently, when the MCP thickness and operating voltage are fixed, an optimum pore radius exists to reach maximum gain. Additionally, The simulation of electron tracks in MCP channels reveals that the average acceleration distance before incident inner wall is approximately 20 μm for a curved MCP with applied voltage 950 V, length-diameter-ratio 80:1, and pore diameter 20 μm

Keywords:

MCP, Geant4, Monte Carlo, Furman model, SEY

¹Email: yanbj@ihep.ac.cn

²Email: miaohan@ihep.ac.cn

1. Introduction

MCP is a widely used detector. Its applications cover high energy and nuclear physics[1, 2, 3, 4], mass spectrometry [5, 6] and image intensifier [7, 8]. MCP is composed of millions of array channels, and can have a thickness of less than 1 mm. Therefore, MCP offers 2-dimensional image resolution and higher time resolution than traditional dynode electron multiplier [9]. Nowadays, many physical experiments propose a higher performance demands, such as a higher signal-to-noise ratio. After-pulse, a type of noise caused by residual molecules in the vacuum device, cannot be ignored in some high-sensitivity experiments [10]. Specifically, as the avalanche of electrons in MCP, there are lots of secondary electrons at the end of channel. Some molecules where are in channel will be ionized by these secondary electrons. The ionized positive ions are accelerated towards the cathode by the applied electric field. Furthermore, some secondary electrons will be produced by those positive ions collision around cathode. Under the force of electric field, the electron that is generated by positive ions will undergo multiplication procedure once again and lead to another output signal, which is called after-pulse. Commonly, after-pulse delays in hundreds of nanoseconds to tens of microseconds to initial pulse[10]. To suppress after-pulse, according to the generation mechanism of the after-pulse, we can increase the vacuum degree of the MCP working environment. Another useful method is using chevron or curved channels MCP. Because of the shape of channel, the ions are difficult to track back to cathode to excite new electrons. In fact, chevron channels MCP is consisted of two straight channel MCP. However, because of manufacture craft limited, it is inevitable that there will exist a gap between two piece of MCP. The electrons are likely to diffused as going through the gap. Consequently, the diffusion leads to deterioration of peak-to-valley ratio and resolution for MCP. However, there is no gap in curved channel MCP. Theoretically, the curved channel MCP performance is better than chevron channels MCP.

Experimentation is the most straightforward way to study the characteristics of curved channel MCP. However, it is not an efficiency and convenient method for most researchers. The theoretical research on MCP multiple processes had been conducted for a long time[11, 12]. However, due to the complexity of secondary electron emission and avalanche amplification, many

model simplify relevant the physic processes, which can only describe a portion of reality[13, 14]. With the advancement of computer performance, numerical simulation has become an important tool in many scientific fields. MCP can also be simulated using the Monte Carlo method with commercial software like CST Studio Suite[15] and SIMION $\text{\textcircled{R}}$ [16]. In this paper, based on the open-source software Geant4, we simulate the entire process of electron multiples in MCP channel. Thanks to the Geant4 open-source license, we can modify the source and add necessary modules. For the core physic process of secondary electron emission, we refer to Furman model [17], and made minor modifications to meet our needs.

In Section 2 we introduce the basic theory of secondary electron emission and discuss secondary electrons behave in the low-energy range. At the end of Section 2, we make some modifications to the Furman model. In Section 3, we compare the experimental data with the simulation result, and study the effects of various parameters on the performance of curved channel MCP. In section 3.3, we study the electron track in curved channel MCP and analyze the results. And last, we summarize the entire article.

2. Simulation theory and low energy assumption

2.1. Furman model

In this paper, we use Furman model [17] to simulate secondary electron emission process in MCP. The Furman model is a phenomenological model that subjects to energy conservation. Besides, the model uses probability theory to describe the generation of secondary electrons and is mathematically self-consistent [17]. So the Furman model is widely used by Monte Carlo method to simulate Photomultiplier Tube(PMT), MCP detectors[18]. Within the Furman model, the emitted electrons are categorized based on their generation mechanisms, which can be divided into three types, depicted in Figure 1. Backscattered electrons are caused by elastic collision with the atoms of the material. In this process, there is little energy transfer, resulting in backscattered electron emission energy being close to primary electron energy. Rediffused electrons, on the other hand, are generated through inelastic collisions with material atoms. Compared with collisions, inelastic collisions involve significant energy transfer. As a result, the energy of rediffused emission ranges from 0 eV to primary electron energy. True secondary electrons mainly response for electron avalanche in micro-channel. When the primary electrons penetrate material surface, partial energy will deposit in the solid,

exciting other electrons. These excited electrons may diffuse to the surface and emit to the free space.

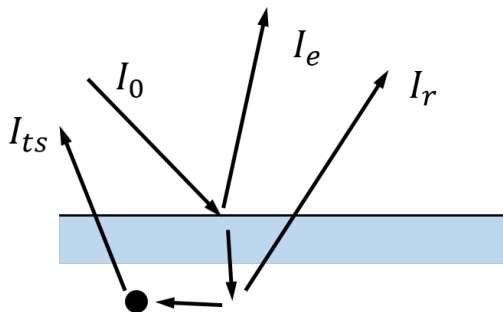


Figure 1: The diagram of three types secondary electron emission process. I_0 represents incident electron, I_e represents the backscatter electron, I_r represents the rediffused electron and I_{ts} represents the true secondary electron.

Secondary electron yield(SEY) and energy spectra of secondary electrons are two important physical quantity that can describe the process of secondary electron emission[19, 20, 21]. The SEY, denoted as δ , quantifies the capacity of a material to emit secondary electrons, defined in Equation 1.

$$\delta = \frac{I_s}{I_0} \quad (1)$$

I_0 represents the number of incident electron and I_s represents the number of the emission electron from material surface. . For the electron multiplier device, a SEY value larger than 1 is typically desired. Base on the δ , the emitted-energy spectrum is $d\delta/dE$ [17].

In the Furman model, we use some empirical formulas to describe SEY and energy spectra of secondary electrons. In fact, these formulas are non-unique[22] and the parameters they involve do not have physical significance. However, they are convenient for sampling in Monte Carlo methods and have good fitting to experiment data.

Equation 2, 4 and 5 correspond to true secondary electron yield, backscatter secondary electron yield and rediffused secondary electron yield , respectively[19, 20]. In equation 2, the $\delta_{ts}(E_0, \theta_0)$ denotes true secondary electron yield when incident electron energy is E_0 and incident angle is θ_0 . In the $D(x)$ function, s is a parameter that control curve shape. Furthermore, when $x = 1$, the $D(x)$ reaches its maximum value. In other words, when incident electron

energy is $\hat{E}(\theta_0)$, SEY value is maximum $\hat{\delta}(\theta_0)$, like in Figure 2 .

$$D(x) = \frac{sx}{s-1+x^s} \quad (2)$$

$$\delta_{ts}(E_0, \theta_0) = \hat{\delta}(\theta_0) D \left[E_0 / \hat{E}(\theta_0) \right]$$

Under the specify incident energy, SEY also will be changed by the incident angle. It can be described by equation 3. t_1, t_2, t_3 and t_4 are all fit parameters. The Figure 3 shows SEY curves in different incident angle.

$$\hat{\delta}(\theta_0) = \hat{\delta}_{ts} [1 + t_1 (1 - \cos^{t_2} \theta_0)] \quad (3)$$

$$\hat{E}(\theta_0) = \hat{E}_{ts} [1 + t_3 (1 - \cos^{t_4} \theta_0)]$$

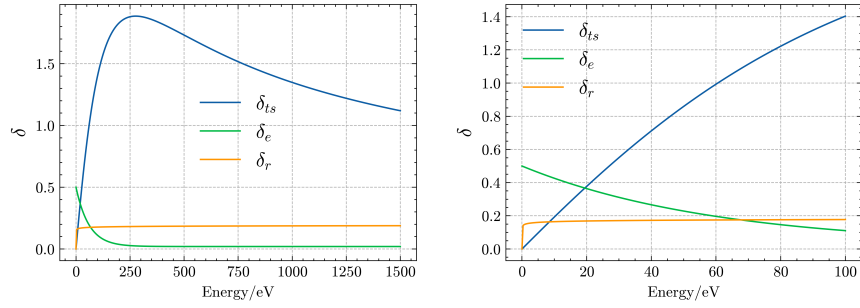
In equation 4, δ_e denotes backscatter electron yield, while in equation 5, δ_r represents rediffused electron yield. All parameters in these equations, except for E_0 , which is the incident energy, are fitting parameters. From Figure 2(a) and Figure 2(b), we can find that the proportion of backscatter electron is high in low energy region and decrease to $P_{1,e}(\infty)$ as the incident energy increase. The rediffused electron yield remains relatively flat in the region of interest.

$$\delta_e(E_0, 0) = P_{1,e}(\infty) + \left[\hat{P}_{1,e} - P_{1,e}(\infty) \right] e^{-(|E_0 - \hat{E}_e|/W)^{p/p}} \quad (4)$$

$$\delta_r(E_0, 0) = P_{1,r}(\infty) \left[1 - e^{-(E_0/E_r)^r} \right] \quad (5)$$

2.2. Electron field calculation

In electron optical simulations, the accuracy of electric field calculation has a significant effect on simulation result. In this paper, focusing on MCP simulation, the main objective is to accurately solve the generalized Poisson equation[23], as shown in equation 6. The potential, denoted as V, is the quantity we aim to solve for. ρ is charge density. In MCP model, there is no free charge distribution in domain of interest. So the ρ is constant 0. ϵ_0 is vacuum permittivity and $\epsilon(\mathbf{r})$ denotes relative permittivity, which may be a function of position if the material is nonuniform. The most commonly used numerical method to solve this equation is finite difference method (FDM) with structured grids. However, when the dielectric material was suddenly



(a) Three types secondary electron yield curve. (b) Three types secondary electron yield curve zoomed in 0 to 100 eV.

Figure 2: Empirical formula depicts secondary electron yield for different processes.

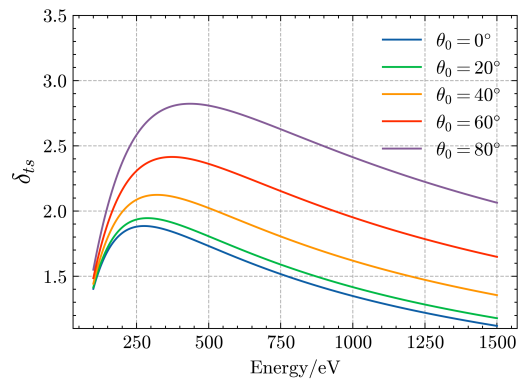


Figure 3: SEY curves under different incident angle.

changed, mathematically, the permittivity ϵ becomes discontinuous, and the FDM may not work well in such cases. Above all, we choose Finite Element Method(FEM) to solve space electron field. The FEM converts generalized poisson equation into a weak form, as shown in equation 7. In this equation, Ω represents domain to be solved. S_k and S_g are the boundaries of domain. E_n denotes the component of the electric field in the S-plane direction. v is called basis functions in FEM[24]. Commonly, FEM requires subdividing the domain into unstructured grid, which can adapt to complex geometric domains. We use the open source software Gmsh to subdivide domains that to be solved. It contains many C++ or python interface that we can embed the Gmsh into Geant4 or python code[25].

$$\nabla \cdot [\epsilon(\mathbf{r})\nabla V(\mathbf{r})] = -\frac{\rho(\mathbf{r})}{\epsilon_0} \quad (6)$$

$$\int_{\Omega} (\nabla v)^T \epsilon \nabla V \, d\Omega = - \int_{S_k} v E_n \, dS - \int_{S_g} v \nabla V \, dS + \int_V v \rho \, d\Omega \quad (7)$$

$$V = \phi \text{ on } S_g$$

2.3. Low energy region assumption

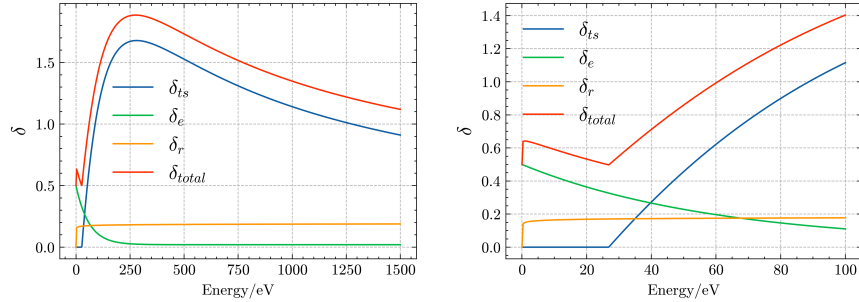
In fact, regardless of the true secondary electron emission mechanism, according to conservation of energy, there must be a certain energy threshold for the excited electron to overcome the surface potential energy of the material. This can be compared to the photoelectric effect. As we know that when photon frequency below threshold frequency, there is no electron can overcome surface potential to emission. Similarly, the true secondary electron can only be emitted when the primary electron energy is above a specify value.

In Furman model, equation 2 shows good agreement with experimental data for incident energy above 100 eV. However, based on the above understanding, we can conclude that the true secondary electron curve does not pass through the origin (0, 0) point. As the incident energy decrease, the true secondary electron yield decreases and reaches 0 when the incident energy decrease below a certain value. Therefore, we need to modify the SEY curve.

From Figure 2, we can find that in the high energy region (incident energy $> 100\text{eV}$), backscatter electron yield and rediffused electron yield are approximately constant. This suggests that the shape of true secondary elec-

tron yield curve is similar to the total secondary electron yield curve above 100 eV. We can use equation 2 to fit the total yield and obtain δ_{total} . To acquire true yield, we subtract δ_e from δ_{total} then subtract δ_r . Finally, we get the new equation 8 to describe true secondary yield. The function curve is showed in Figure 4.

$$\delta_{ts} = \begin{cases} \delta_{total} - \delta_e - \delta_r & \delta_{ts} > 0 \\ 0 & \delta_{ts} < 0 \end{cases} \quad (8)$$



(a) Modified secondary electron yield curve. (b) Modified secondary electron yield curve zoomed from 0 to 100 eV.

Figure 4: Modified furman model SEY curves.

In fact, Baglin et al(2001)[26] have measured the copper sample SEY. The most useful experimental data for our study is about the SEY of copper sample ranges from 4 eV to 30 eV. The data show that the SEY value at 4 eV is about 0.7 and the SEY curve tends to a constant or a bit decrease when the incident electron energy changes from 4 eV to 10 eV. Considering the Figure 4, the SEY curve is slightly decrease under 30 eV, which tendency is similar to the study of Baglin et al(2001). It indirectly support our assumption about low energy region.

3. MCP gain and electron tracks simulation

3.1. Experimental equipment and measurement

To make the simulation results closer to reality, we conducted measurements of the SEY curve for lead glass, which is the main material used in MCP. In our laboratory, we have a spherical vacuum device[27] that can accurately measure SEY of various material, which incident electrons energy

ranges from 100 eV to 1500 eV. In Figure 5, it can be observed that the data points of measured SEY curve are not as smooth as expected. The main reason for this phenomenon is the poor conductivity of the lead glass sample. During the test, it's easy to cause charge accumulation that influences the secondary electron emission. Therefore, compared to good conductors, it's more challenging to accurately measure the SEY of poor conductors. This also bring to another issue. Due to the significant errors encountered in measuring the SEY of lead glass, measuring the secondary electrons energy spectra becomes even more difficult. The energy spectra measurements require the detection of smaller signals, which introduces larger errors. Additionally, in order to acquire different incident energies SEES, we have to measure more data points than SEY measurements. As a result, acquiring the secondary electrons energy spectra of lead glass material becomes a challenging task.

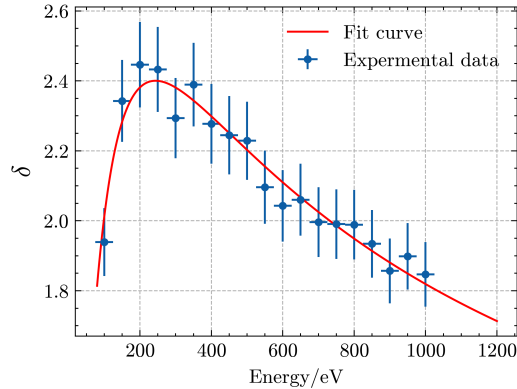


Figure 5: Use equatin 2 to fit experimental data. Fit parameters s is 1.39, $\hat{\delta}(0)$ is 2.40, $\hat{E}(0)$ is 243.71

We have measured the MCP gain at various applied voltage. The experimental setup is illustrated in Figure 6. In a vacuum device, a Tantalum filament, the MCP and an anode were placed sequentially. When the system is working, a current I_s flows through tantalum filament. Some of electrons emitted from the filament will enter the input pore of MCP. The galvanometer G_I measures the input current I_{in} . U_0 applies on MCP. After the avalanche amplification process in MCP channel, we can measure output current from anode. By applying the formula in Equation 9, the MCP gain at the operating voltage was calculated.

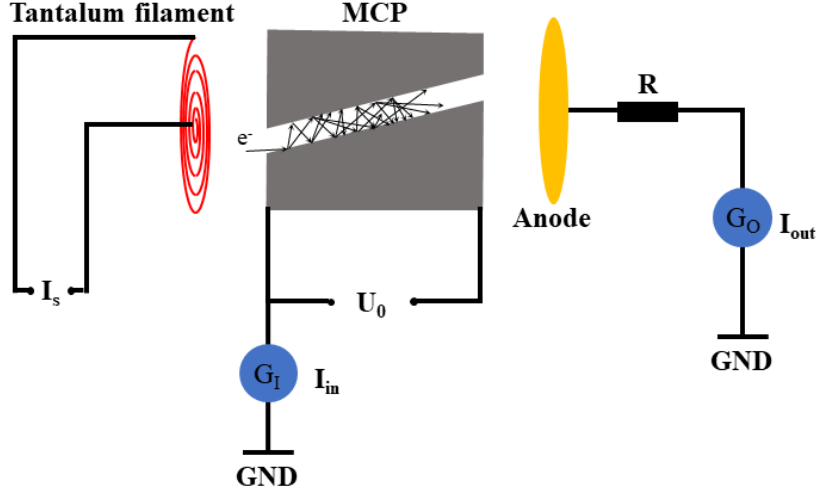


Figure 6: MCP gain testing system diagram.

$$G = \frac{I_{out}}{I_{in}} \quad (9)$$

As mentioned above, it is challenging to directly measure the secondary electron emission spectrum of poor conductor lead glass. However, there are a lot of SEEC data available for other material. The MCP gain characteristic is primarily determined by the material secondary electron mission properties. Therefore, based on the secondary electron energy spectra data of other material and the MCP gain data, by adjusting parameters of energy spectra to iterate simulation process, we can eventually obtain simulation results that are consistent with experimental results. At this point, the energy spectra parameters used in the simulation are close to the real values.

3.2. The simulation of MCP gain versus applied voltage

The gain characteristic of an MCP is not only influenced by the constituent materials but also by its geometric dimensions and applied voltage. Under an optical microscope, we can measure the pore diameter, length-to-diameter ratio of the MCP. By breaking MCP, we can also measure the channel bias angle or other inner geometric dimensions. Based on these actual measurements, in Geant4, the MCP model is established. For the # 1 MCP, the dimensions are provided in Table 1

Table 1: Tested MCP parameters.

Parameter/Unit	# 1 MCP	# 2 MCP
MCP radius/mm	25	24.8
MCP thickness/mm	0.42	0.48
channel radius/ μm	10	6
tilt angle/ $^\circ$	12	5.5
body resistance/ $\text{M}\Omega$	84	90
input current/pA	107	162

After above preliminary steps, we can proceed with running the simulation framework and record calculation results in a root file. In Geant4, we place a sensitive detector(SD) adjacent to the output face of the MCP to capture the output electron kinetic data. When a particle enter the SD, we terminate the particle and halt any further calculations related to it in order to conserve computing resources. So no particle can go through the SD, and we regard all particles are absorbed by SD completely.

We simulate # 1 MCP at different operating voltages. For each simulation run, we randomly beam 1000 electrons onto input face of MCP and record the output electron’s data in a root file. By analyzing the number of electrons in the root file, we can figure out the average gain at each specify operating voltage. We sweep the voltage range from 700 volts to 1200 volts and obtain the voltage-gain curve, as shown in Figure 7. Similarly, we also simulate # 2 MCP with the same SEY parameters and SEES parameters. The resulting gain-voltage curve for #2 is shown in Figure 8.

From the two curves presented above, we can find that there is a significant exponential relationship between gain and applied voltage. It is consistent with other reference paper[12]. However, this exponential relationship also leads to a computational challenge. As the applied voltage increases, the number of particles that need to be simulated and calculated also increase exponentially.

Furthermore, we find that the Monte Carlo results are in good agreement with experimental data. However, when a sufficiently high operating voltage

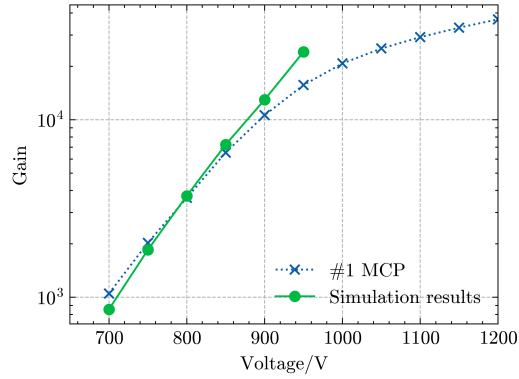


Figure 7: #1 MCP gain versus applied voltage curve. The x markers denote measurement data. The circle markers denote simulation data.

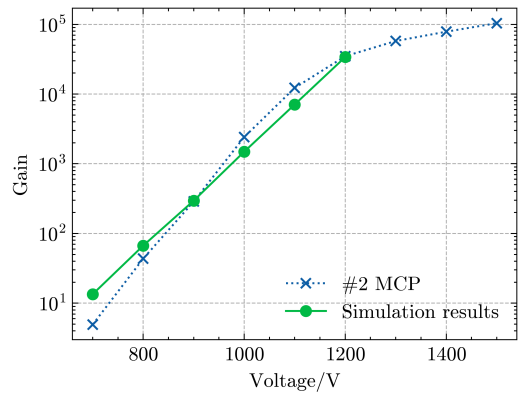


Figure 8: #2 MCP gain versus applied voltage curve. The x markers denote measurement data. The circle markers denote simulation data.

is applied, the MCP is under saturation effect, leading to a suppression of the gain. At this point, the gain and voltage no longer follow an exponential relationship and tend to stabilize at a constant value. In Geant4 Monte Carlo simulation, the space charge effect is not taken into account. As a result, the simulated gain continues to increase as the voltage rises exponentially. From the Figure 7 and 8, it is obvious that the gap between experimental data and simulation data become larger in high voltage region.

In addition to the straight channel MCP, we also do some simulations on curved channel MCP. The model is showed in Figure 9. These MCPs are designed to effectively reduce after-pulses[28], which are the main source of noise in high-sensitivity experiments[29, 30, 31]. In our study, We investigated various geometry parameters, such as channel curvature radius, channel length-to-radius ratio and channel pore radius. Similar to the previous simulations, we beamed 1000 electron onto MCP input face and recorded output electrons data. The resulting gain-voltage curve for the curved channel MCP is shown in Figure 10. As expected, the gain still increase with operating voltage following an exponential law.

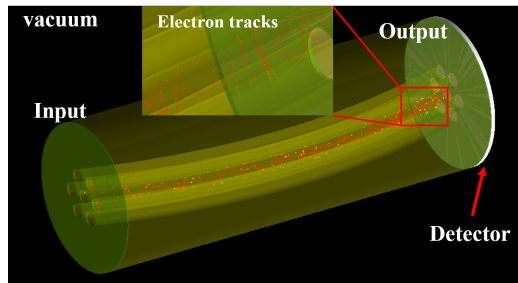


Figure 9: Curved channel MCP model in Geant4. Only parts of electron tracks is shown in figure

By varying the curvature radius of channel, we simulated the MCP gain at different operating voltages. The simulation results, as shown in Figure 10, indicate that the curvature radius of channel has little effect on gain. However, the pore radius has a significant effect on it. To further understand the impact of the pore radius on MCP gain, we simulate the MCP gain with different pore radius while keeping the MCP thickness and operating voltage fixed. Figure 11 demonstrates that there exists an optimal pore radius that maximizes MCP gain.

We can use a simple model to illustrate the variation trend of gain with

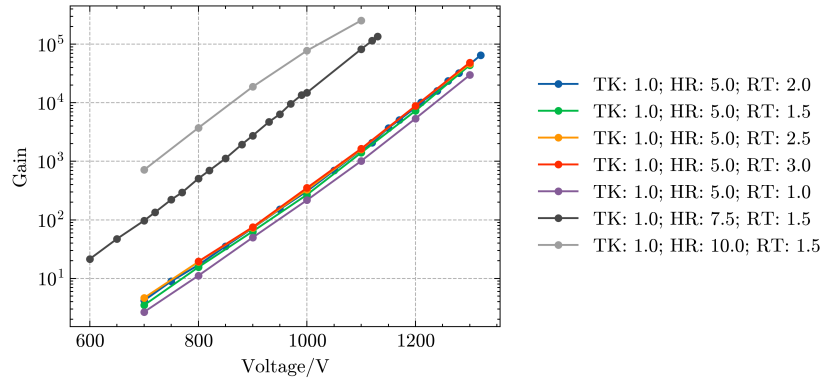


Figure 10: The relationship of gain and applied voltage under different geometry parameters. TK represents MCP thickness, the unit is millimeter. HR denotes MCP channel pore radius, its unit is micrometer. RT denotes curved channel radius, its unit is millimeter

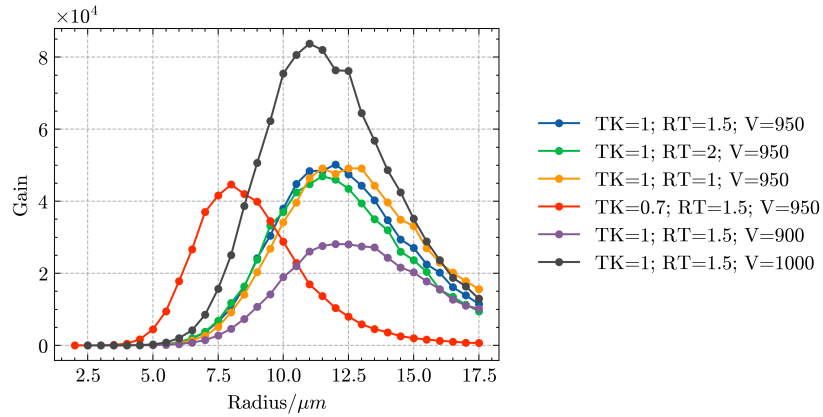


Figure 11: The relationship between gain and channel pore radius. TK and RT respectively represent thickness of MCP and curved channel radius, and the unit is millimeter. V denotes applied voltage on MCP, its unit is volt.

pore radius when the MCP thickness and operating voltage are fixed. We can consider the electrons avalanche in the MCP channel and the incident points are continuous distribution along the inner channel. To simplify the problem [12, 14], we regard the MCP multiplication process as discrete dynode multiplication process. We assume that the MCP is equivalent to a PMT with N dynodes, and the average SEY is represented by δ . Therefore, it can approximately calculate the MCP gain as $G = \delta^N$. The MCP pore radius can effect both N and δ . When the pore radius is expanded, the electrons will take a longer time to travel from one side of the inner wall to the other side. It leads to electron move further in the axial direction. While, the number of dynodes N will decrease, and the electrons obtain more energy from the electric field, leading to an increase in incident energy, the average δ value becomes bigger. So an increase in pore diameter affects both N and δ . Figure 11 demonstrates that as the pore radius increase, the MCP gain also increase until it reaches the peak. At this point, the growth of δ dominates above equation reference to G , leading to an increase in gain. After MCP gain reaches the peak, as the pore radius continues to increase, the decrease in variable N becomes dominant in above formula about G , resulting in a decrease in MCP gain.

In this section, we use Geant4 to simulate both straight channel MCPs and curved channel MCP. The straight channel MCP simulation mainly aimed to calibrate SEEC parameters. Through multiple iterations, we obtained appropriate parameters that could accurately describe the secondary electron emission properties of the MCP's inner wall material. For curved channel MCP, we studied the influence of geometric parameters on the gain. In conclusion, the curvature radius has little effect on the MCP gain, allowing us to increase the channel curvature to suppression after-pulses. Additionally, the research of pore radius shows that when the MCP thickness and operating voltage are fixed, adjusting the pore radius can effectively optimize the MCP gain.

3.3. The simulation of electron tracks in MCP channel

In fact, as a Monte Carlo simulation software framework, Geant4's main task is to track the trajectories of particles and sample various types of reactions. This allows us to easily to analyze electrons behavior in the MCP channel, which is nearly impossible to observe in experiment. We set parameters for the curved channel MCP as listed in Table 2, and apply a voltage of 950V. When a single electron incident in the MCP channel, we can obtain

over 10^5 track data by the action hook class in Geant4. According to these track data, we can uncover some novel insights.

Table 2: Tested MCP parameters.

Parameter/Unit	Curved channel MCP
MCP thickness/mm	1
channel radius/ μm	10
Applied voltage/V	950
Channel curvature radius/mm	1

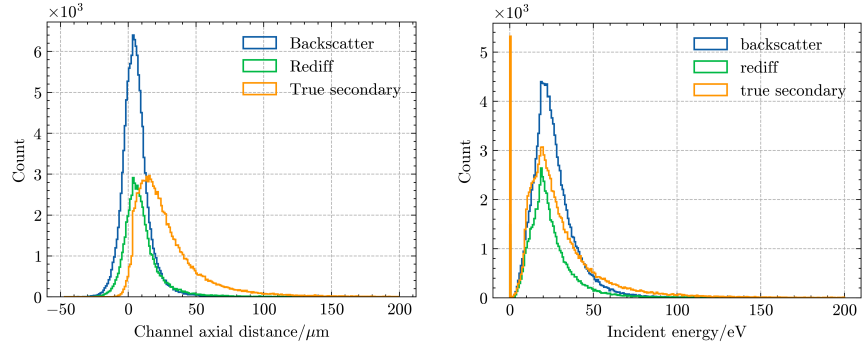
From Figure 12(a), we can find that even under the 950V operating voltage, the average axial jump distance of electrons is approximately 20 μm . It's a deviation from what was previously believed. Many papers[14, 32] compare the MCP multiplication process to a dynode PMT, where most of electrons undergo about 10 times multiplication steps, with each step SEY value is about 2-3. However, our simulation results show that the electron jump distance in channel is about 20 μm . In a 1 mm thick MCP, the total number of multiplications is about 50. To achieve a gain of 10^5 , the average electron yield is about 1.1.

Figure 12(b) shows the incident energy of electrons in channel, which is as expected to be around 30 eV on average. This energy is slightly higher than the threshold energy $\delta = 1$ in SEY curve. According to the Figure 4, these electrons are most likely to take part in backscattering. Only a small proportion of electrons have a significant effect on the multiplication process.

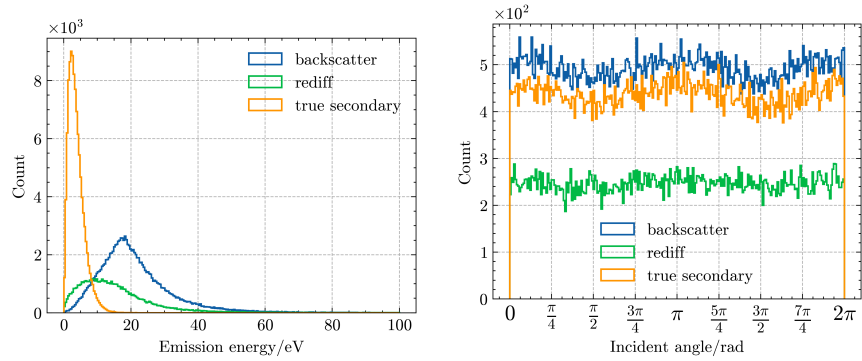
The vertex distribution in Figure 12(c) shows the energy of electrons emitted from the MCP inner wall. There are three peaks. The left side peak corresponds to the true secondary electrons, as the true secondary electron emitted energy is approximately independent of the incident energy. The right side wider peak corresponds to the contribution from backscatter electrons. The peak that is sandwiched between the two peaks corresponds to rediffused electrons.

Lastly Figure 12(d) suggests that the electron motion in the channel is not isotropic. We can find that electrons tend to bombard in a direction parallel to the plane where the channel bends. This tendency leads to the output electron

distribution in a elliptic, rather than a circular distribution.



(a) Electron axial distance distribution in MCP channel. (b) Energy distribution of electron impact on channel inner wall.



(c) Secondary electron emission energy distribution. (d) Secondary electron directional distribution in channel.

Figure 12: MCP electron track.

In this section, we research the electrons behavior in MCP channel by Geant4. By analyzing the simulation results, it shows that the electrons average axial jump distance is shorter than what we expected before. At the same time, to achieve the gain that is measured in experiment. Most of electrons undergo 50-60 times collision for a MCP whose length-diameter ratio is around 50. To sum up, the electrons in MCP are in a state, which is the majority electrons are not accelerate fully, and the average yield that these electron is only a slightly larger than 1.

4. Conclusion

According to our simulation result, we can find that the curved channel MCP gain increase with applied voltage exponentially before reaching to saturation. Additionally, when the MCP thickness and operating voltage are fixed, the MCP gain is significantly affected by the diameter of MCP pores . For instance, when MCP applied 950V and the thickness of MCP is 1 mm. It's optimum diameter is about 20 μm .

Furthermore, by analyzing the electron track data in the MCP channel (as shown in Figure 12), we can conclude that the acceleration distance of electrons in the channel is so short that leads to particle energy that bombard channel inner wall is low. Consequently, only a few electrons can generate true secondary electrons, while the majority of them undergo backscatter. From this perspective, enlarging the pore diameter can increase the MCP gain. In fact, under fixed thickness and operating voltage conditions, we can determine the optimal pore diameter by using the simulations.

Acknowledgements

This work was supported by the National Natural Science Foundation of China (Grant 11975017), the State Key Laboratory of Particle Detection and Electronics (SKLPDE-ZZ-202215). We are grateful to Dr. Kaile Wen for his insightful discussions.

References

- [1] X. You, B. Gao, M. Chen, H. Li, C. Liu, K. Li, et al., The application of 20 inch mcp-pmt in lhaaso-wcda, *Nonlinearity* (1800) 10.
- [2] B. Gao, C. Liu, L. Liu, M. Chen, K. Lia, X. Youa, Pos (icrc2023) 801 the charge response study of lhaaso-wcda large spherical pmts (2023).
- [3] Q. Wu, Y. Cao, G. Huang, M. Jin, Z. Jin, D. Li, S. Liu, L. Ma, S. Qian, L. Ren, et al., The design of large area mcp-pmt for neutrino detector, in: *PARTICLE PHYSICS at the Year of 150th Anniversary of the Mendeleev's Periodic Table of Chemical Elements: Proceedings of the Nineteenth Lomonosov Conference on Elementary Particle Physics*, World Scientific, 2021, pp. 139–143.

- [4] Y. Chang, G. Huang, Y. Heng, D. Li, H. Liu, S. Liu, W. Li, Z. Ning, M. Qi, S. Qian, et al., The r&d of the 20 in. mcp-pmts for juno, Nuclear Instruments and Methods in Physics Research Section A: Accelerators, Spectrometers, Detectors and Associated Equipment (2016) 143–144.
- [5] M. Nishiguchi, M. Toyoda, M. Ishihara, M. OHTAKE, T. SUGIHARA, I. KATAKUSE, Development of a miniature double focusing mass spectrograph using a focal plane detector, Journal of the Mass Spectrometry Society of Japan 54 (1) (2006) 1–9.
- [6] D. Klumpar, E. Möbius, L. Kistler, M. Popecki, E. Hertzberg, K. Crocker, M. Granoff, L. Tang, C. Carlson, J. McFadden, et al., The time-of-flight energy, angle, mass spectrograph (teams) experiment for fast, The FAST Mission (2001) 197–219.
- [7] A. Tremsin, J. McPhate, J. Vallerga, O. Siegmund, J. Hull, W. Feller, E. Lehmann, Detection efficiency, spatial and timing resolution of thermal and cold neutron counting mcp detectors, Nuclear Instruments and Methods in Physics Research Section A: Accelerators, Spectrometers, Detectors and Associated Equipment 604 (1-2) (2009) 140–143.
- [8] G. Fraser, A. Brunton, J. Lees, J. Pearson, W. Feller, X-ray focusing using square-pore microchannel plates first observation of cruxiform image structure, Nuclear Instruments and Methods in Physics Research Section A: Accelerators, Spectrometers, Detectors and Associated Equipment 324 (1-2) (1993) 404–407.
- [9] B. Leskovar, Microchannel plates, Physics Today 30 (11) (1977) 42–49.
- [10] A. Abusleme, T. Adam, S. Ahmad, R. Ahmed, S. Aiello, M. Akram, A. Aleem, T. Alexandros, F. An, Q. An, et al., Mass testing and characterization of 20-inch pmts for juno, The European Physical Journal C 82 (12) (2022) 1168.
- [11] E. Baroody, A theory of secondary electron emission from metals, Physical Review 78 (6) (1950) 780.
- [12] J. Adams, B. Manley, The mechanism of channel electron multiplication, IEEE Transactions on Nuclear Science 13 (3) (1966) 88–99.

- [13] D. Loubet, C. Barat, Mechanism of secondary electron multiplication within a curved channel multiplier, *Nuclear Instruments and Methods* 111 (3) (1973) 441–444.
- [14] E. H. Eberhardt, Gain model for microchannel plates, *Applied Optics* 18 (9) (1979) 1418–1423.
- [15] D. Systèmes, Cst studio suite: Electromagnetic field simulation software, <https://www.cst.com/> (2022).
- [16] L. Scientific Instrument Services (SIS) by Adaptas Solutions, Simion: The field and particle trajectory simulator, <https://simion.com/> (2022).
- [17] M. Furman, M. Pivi, Probabilistic model for the simulation of secondary electron emission, *Physical review special topics-accelerators and beams* 5 (12) (2002) 124404.
- [18] L. Guo, P. Chen, L. Li, Y. Gou, H. Liu, Z. Liu, L. Xin, J. Tian, Numerical simulation study on gain nonlinearity of microchannel plate in photomultiplier tube, *IEEE Transactions on Nuclear Science* 68 (12) (2021) 2711–2716.
- [19] H. Bruining, *Physics and Applications of Secondary Electron Emission: Pergamon Science Series: Electronics and Waves—a Series of Monographs*, Elsevier, 2016.
- [20] P. A. Redhead, J. P. Hobson, E. V. Kornelsen, *The physical basis of ultrahigh vacuum*, Springer, 1968.
- [21] G. van Eden, D. Verheijde, J. Verhoeven, Secondary electron emission yield measurements of dielectrics based on a novel collector-only method, *Nuclear Instruments and Methods in Physics Research Section B: Beam Interactions with Materials and Atoms* 511 (2022) 6–11.
- [22] M. Wu, C. A. Kruschwitz, D. V. Morgan, J. Morgan, Monte carlo simulations of microchannel plate detectors. i. steady-state voltage bias results, *Review of Scientific Instruments* 79 (7) (2008).
- [23] J. R. Nagel, et al., Solving the generalized poisson equation using the finite-difference method (fdm), *Lecture Notes*, Dept. of Electrical and Computer Engineering, University of Utah (2011).

- [24] S. Mazumder, Numerical methods for partial differential equations: finite difference and finite volume methods, Academic Press, 2015.
- [25] C. Geuzaine, J.-F. Remacle, Gmsh: A 3-d finite element mesh generator with built-in pre-and post-processing facilities, International journal for numerical methods in engineering 79 (11) (2009) 1309–1331.
- [26] V. Baglin, G. Vorlauffer, N. Hilleret, I. Collins, B. Henrist, A summary of main experimental results concerning the secondary electron emission of copper, Tech. rep. (2001).
- [27] K. Wen, S. Liu, B. Yan, Y. Yu, Y. Yang, Spherical measuring device of secondary electron emission coefficient based on pulsed electron beam, in: Proceedings of International Conference on Technology and Instrumentation in Particle Physics 2017: Volume 1, Springer, 2018, pp. 113–116.
- [28] D. S. Evans, Low energy charged-particle detection using the continuous-channel electron multiplier, Review of Scientific Instruments 36 (3) (1965) 375–382.
- [29] J. collaboration, et al., Juno physics and detector, Progress in Particle and Nuclear Physics 123 (2022) 103927.
- [30] E. Marzec, J. Spitz, Neutrino decoherence and the mass hierarchy in the Juno experiment, Physical Review D 106 (5) (2022) 053007.
- [31] K. Jiang, Z. Tang, X. Li, C. Li, Study of the water Cherenkov detector with high dynamic range for LHAASO, Journal of Instrumentation 15 (08) (2020) C08021.
- [32] L. Harris, Saturation in continuous channel electron multipliers, Review of Scientific Instruments 42 (7) (1971) 987–992.